The Pennsylvania State University

The Graduate School

Department of Electrical Engineering

RESONANCE RAMAN SPECTROSCOPY IN THE ULTRAVIOLET USING A TUNABLE LASER

A Dissertation in

Electrical Engineering

by

Adam H. Willitsford

Submitted in Partial Fulfillment
of the Requirements
for the Degree of

Doctor of Philosophy

August 2008

The dissertation of Adam H. Willitsford was reviewed and approved* by the following:

C. Russell Philbrick
Professor of Electrical Engineering
Thesis Advisor
Chair of Committee

Stewart Kurtz
Professor of Electrical Engineering

Kultegin Aydin
Professor of Electrical Engineering

Sven G. Bilén
Associate Professor of Electrical Engineering

H. Nels Shirer
Associate Professor of Meteorology

Zhiwen Liu
Assistant Professor of Electrical Engineering

Hans Hallen
Professor of Physics North Carolina State University
Special Member

W. Kenneth Jenkins
Professor of Electrical Engineering
Head of the Department of Electrical Engineering

*Signatures are on file in the Graduate School

ABSTRACT

The characterization of minor atmospheric constituents, such as pollutants, bio-hazards, and other rogue materials has been a difficult task for the research community. Raman scattering techniques have been employed to detect and identify materials in both a laboratory and field settings; however, Raman scattering processes have an extremely small scattering cross section; however, which limits its utility. Through the use of the resonance enhancement it is possible to extend the utility of the Raman scattering technique.

This dissertation presents a novel Raman scattering experiment that was designed and developed in collaboration with the research group of Professor Hans Hallen and performed at The North Carolina State University Optics Lab. Measurements of resonance-enhanced Raman scattering were made on multiple samples. In particular, this dissertation reports an investigation of the phenomenon of resonance-enhanced Raman scattering in two aromatic hydrocarbons: benzene and toluene.

Algorithms were developed for the analysis of the Raman data that included removing the noise background and normalizing data to remove fluctuations in laser power and detector efficiencies. An algorithm for calculating the resonance gain was developed and applied to both benzene and toluene. The resonance-enhanced Raman scatter of benzene and toluene was found to be 100-10,000× larger than their normal Raman scattering spectrum when the molecules are excited by radiation at peaks in their respective electronic resonance excitation bands. Further analysis of the resonant Raman spectra of benzene was performed, and the Raman scattered lines

observed were assigned to the modes of vibration. The resultant spectra are in good agreement with the earlier work performed by Zeigler and Hudson[1981] and Asher [1984].

The original goal of the investigation of the resonance enhancement was to seek seek improved capability for lidar based on the experiments. It can be argued that the absorption of energy in the energetic double bonds of carbon which form the benzene ring can be used for resonance Raman enhanced scatter, and future investigations should result in demonstrations of our ability to remotely detect a number of interesting species.

Several achievements from my research described in this dissertation include:

1) A new experiment has investigated resonance-enhanced Raman scattering for the first time using small steps in excitation wavelength [~ 0.12 nm].
2) Excitation at wavelengths in the ultraviolet spectrum resulting in resonance-enhanced Raman scattering in both benzene and toluene occur over extremely narrow wavelength bands.
3) A high resolution (fine-tuning) of the ultraviolet excitation has been used to investigate the enhancement, and to isolate the gain region for resonance-Raman scattering in benzene.
4) The peak resonance enhancement is found to correlate with the vapor-phase absorption peaks of both benzene and toluene, when the experiments were performed in liquid phase.

5) The resonance Raman spectra of benzene has been analyzed and vibrational modes associated with the scattering have been assigned.
6) An algorithm is described for use in the analysis of the Raman spectra, including noise removal and normalization corrections for source and detector wavelength dependence, and it is applied in analyzing the data collected.
7) An algorithm was developed for the calculation of the resonance enhancement to determine the gain factor for the resonance Raman scattered signals.

TABLE OF CONTENTS

LIST OF FIGURES

LIST OF TABLES

ACKNOWLEDGMENTS

Thank you to all the faculty, friends, and family members who have helped me to complete not only this dissertation but another step in my lifelong learning process. Each deserves thanks:

Thank you to my thesis advisor C. Russell Philbrick. Dr. Philbrick has been a wonderful mentor, role model, and friend throughout my graduate career. Dr. Philbrick has taught me to "paint the picture" and see the forest for the trees without losing track of the details. I am forever grateful for the experience and diverse opportunities that I was afforded while working with Dr. Philbrick. The knowledge, skills, and thoughtfulness that he has imparted to me will be forever cherished.

Thank you to Dr. Hans Hallen of the North Carolina State University Physics Department. During the experimental portion of my dissertation, I worked hand-in-hand with the Optics Lab at NC State. I was welcomed with open arms into Dr. Hallen's lab and found I quickly felt like a member of the "Wolf Pack". Dr. Hallen quickly became another mentor and friend whose knowledge in optics, mechanics, and experimental design were paramount.

Thank you to Dr. Stewart Kurtz for his ever-present optimism and excitement. It was his passion for the study of benzene that moved my experiments forward. I had limited success with water as a resonant material, and Dr. Kurtz urged me to characterize benzene, the results of which are detailed in this dissertation. His wealth of knowledge on benzene and its structure have proven to be of great help.

Thank you to Todd Chadwick, the only other person who truly understands the trials and tribulations of using a tunable OPO. During my time at NC State, Todd and I worked extensively to create a novel and successful resonance experiment. He and I spent many, many long hours in the lab aligning, tweaking, breaking, building, and reconstructing various portions of the resonance Raman experiment. The opportunity to bounce ideas and thoughts off of Todd was of incalculable value. Todd is a brilliant physicist who understands hard work as well as the need for stress relief. The nightly exercise, be it at the gym or on the tennis court was a wonderful respite from the laboratory atmosphere. His friendship became a shining light during the dissertation process.

Thank you to the members of the Penn State University Lidar Lab. Thanks to Dave Brown for his continued hard work and friendship throughout our time together at Penn State. Also thanks to the other members of the PSU Lidar lab: Joe Begnoché, Jason Collier, Perry Edwards, Guangkun (Homer) Li, Jin Park, Sameer Unni, Sachin Verghese, and Andrea Wyant.

Thank you to the members of the North Carolina State University Optics Lab who helped me to feel at home during my visit. Special thanks to Ryan Neely for his friendship, computer expertise, and electrical wiring prowess. Thank you also to Robert Daniels for making me feel at home in North Carolina.

Thank you to the members of my Ph.D. committee for their constructive criticism and feedback: Dr. C. Russell Philbrick, Dr. Hans Hallen, Dr. Stewart Kurtz, Dr. Kultegin Aydin, Dr. Sven Bilén, Dr. Zhiwen Liu, Dr. Nels Shirer, and Dr. Kenneth Jenkins.

Thank you to Michigan Aerosphace Corporation for their generous loan of the EMCCD camera. Thank you to Diane Knight for loaning us the diamond that was so important during the calibration of the experiment.

Thank you to Dr. Craig Bohren of Penn State and Dr. Sanford Asher of the University of Pittsburgh, and Dr. Arthur Sedlacek of Brookhaven National Lab, for their constructive input and feedback during the investigation.

Thank you to my all my 'gym buddies' for their inspiration and perspiration during the many needed hours of stress relief. Also thank you to my good friend Cory Smith, with whom I have spent many hours both in the gym and on the running road sharing ideas, thoughts, and stories.

Thank you to all my friends at Centre Soccer with whom I enjoyed hours and hours of fun on and off the field, giving me a much needed break from what they have dubbed the "Laserology" lab. Thank you to Mike Renz for your friendship and generosity, and for always keeping me honest and humble.

Thank you to Dr. Neil and Marlene Stringer who have provided me with continued support and encouragement throughout my time at Penn State. They have been a wonderful source of knowledge and experience that has helped me to grow and learn. Thank you to Marlene for your help with editing many of my writings. Thank you to my sisters-in-law, Elizabeth and Katharine Stringer, who exude laughter and love. Thank you to my brother-in-law, Daniel Stringer, for his support, friendship, and grilling mastery.

Thank you to my brother, Noah Willitsford, for the love and support he has given me throughout my life. From the time we were kids it was always wonderful to have a partner-in-crime;I could not have asked for a better brother.

Special thanks to my parents, Mr. David and Brenda Willitsford, who have provided me with continuous love, support, and encouragement throughout my life. They have given me everything that I could ever need to succeed and I am forever in their debt.

Special thanks to my wife, Abigail Stringer, who has made my life complete. She has been the proverbial light at the end of the tunnel, supporting me, loving me, and helping me in every aspect of my graduate career. She has shown me the meaning of hard work, and I have done my best to emulate her work ethic during this journey.

Chapter 1:
Introduction

The need for improved techniques for measuring chemical species has never been more pronounced. The problems in need of attention include monitoring air pollutants, obtaining additional evidence for global warming, measuring toxins, detecting and measuring chemical-biological agents, and finding explosive materials due to the threat of international terrorism.

Improvements also are needed for the measurements and studies of greenhouse gas pollutants. These gases are found most commonly in small concentrations, which are either spread throughout the atmosphere in the case of pollutants, or are found in low concentrations around a small source such as an explosive material or toxic chemical. Detection, identification, and quantification of trace constituents spread throughout the atmosphere are posing a challenge to the research community. Currently, point measurements from balloon sondes and ground-based systems provide high quality measurements of the local atmosphere; they are poor in spatial and temporal resolution however.

Lidar has made it possible to measure and analyze the atmospheric constituents with increased spatial and temporal resolution [Alpers *et al.*, 2004; Inaba, 1976; Kobayasi and Inaba, 1970; Measures, 1991; Penney, 1974; Philbrick, 1985; Rosen, 1975; Sedlacek 1995]. Lidar has limitations because it employs Raman scattering for the detection and identification of atmospheric constituents. Although Raman scattering has been used routinely to detect, identify, and quantify molecular concentrations in both laboratory and field settings, the extremely small scattering

cross sections associated with the Raman signals limit the measurements to relatively large concentrations of molecules**.** It is even more difficult to remotely detect and measure unknown chemical species located at significant ranges. Background optical signals in the atmosphere, such as scattered sunlight, also limit the detection. Lidar techniques are often used to detect remotely major atmospheric constituents using their backscattered Raman signal because of the uniqueness of the spectral signature representing each molecular species. In order to extend the utility of lidar remote sensing, a means to enhance the extremely small Raman scattering signals is needed. Some common solutions include simply using more powerful laser transmitters, larger telescope receivers, narrower band filters, and more sensitive detectors; all of these improvements have the capability to enhance the signal-to-noise ratio. There are limits as to how far each technological improvement can be taken however. Another means to enhance the signal-to-noise ratio may be found in using resonance enhancements to increase the Raman scattered signal.

With the advent of more powerful and lower cost tunable ultraviolet sources, it is now possible to consider using the resonance Raman effect on a more routine basis. The resonant enhancement of the scattering intensity occurs as the excitation frequency approaches the energy corresponding to an electronic state of a molecule. This phenomenon has been found to enhance the Raman scattering cross section between 3 and 8 orders of magnitude [Chamberlain *et al.*, 1976]. The increase in sensitivity occurs because of the stronger coupling of optical energy into the molecular vibrational modes. With this increase in Raman scattered signal, it may become possible to detect and quantify significantly smaller concentrations of

chemical and biological species as well as trace pollutants, bio-contaminants, and explosives.

1.1 Goals and Current Work

The primary goal of this thesis is to extend the knowledge and database of the resonant-enhanced Raman scattering effect, so that the technique can be developed for laser standoff detection (lidar) in future measurements of hazardous materials. The work performed in this dissertation finds new features in the resonance enhanced Raman scatter of both benzene and toluene. The enhancement is unique within its extremely narrow enhanced excitation bandwidth of less than 1 nm. This measurement is achieved using the fine-tuning capability of an Optical Parametric Oscillator (OPO) that has a continuous tuning range through the ultraviolet electronic absorption bands between 230 and 300 nm of both benzene and toluene. In most resonance Raman studies, only a few discreet excitation wavelengths are typically chosen, and these are widely separated in significantly large steps (5 nm - 20 nm) [Ziegler, 1980, 1981, 1983; Asher, 1984, 1988, 1993; Gerrity *et al.*, 1985; Sedlacek, 1995]. The large steps in excitation wavelength result from using several common UV laser wavelengths that are readily available. These studies commonly make a point of comparing off-resonance Raman scatter (typically in the visible wavelength region) to near-resonance Raman scatter (typically in the UV wavelength region). Very few studies have actually matched the absorption peak in the molecule of interest; therefore, most investigations never obtain a measure of the resonance

enhancement, but merely a measure of the pre-resonance enhanced Raman scatter signal.

Our investigations using an OPO make it possible to tune the laser with sequential steps as small as 0.12 nm. This fine tuning of the laser center wavelength make it possible to study extremely small changes in excitation wavelength affecting the Raman scatter. Both benzene and toluene exhibited an enhancement in Raman scattered signals on the order of 100 to 10,000×, and the enhancement peak occurred within a narrow range of excitation wavelengths of ± 0.25 nm.

1.2 Outline of Research Accomplishments and Hypothesis

My research work has explored the processes and properties of several interesting molecules to understand the characteristics of the resonance Raman technique. The hypotheses examined in this dissertation are that:

1) The characteristics of the molecular structure, for example the carbon ring, result in a distinct resonance enhancement of Raman scatter associated with the peaks in the absorption spectrum.
2) The resonance enhanced Raman spectra couples significant energy into a number of overtones and combination modes, and additional energy levels are observed in the resonance Raman scattered spectra.
3) Resonance enhanced Raman scattering exhibits a significant increase in the amplitude of spectral features representing the energy states that uniquely identify the molecule. At low concentrations the Raman scattering signal

may be detectable with resonance excitation in the ultraviolet region where absorption is strong.

The primary accomplishments of the research are to:

1) Investigate the processes and properties of the phenomena of pre-resonance and resonance enhanced Raman scatter in two aromatic hydrocarbons: benzene and toluene.
2) Calculate the resonance enhancement gain in the Raman scattered intensity for benzene and toluene.
3) Describe the effects of the resonance enhancement of the Raman spectrum by investigating additional spectral features, including combination and overtones were identified for benzene.

Chapter 2:
A Historical Perspective

Shortly after C.V. Raman's 1928 discovery of the process that we today call Raman scattering [Raman, 1928], Synge proposed the initial concept of optical remote sensing in 1930. He suggested that atmospheric density measurements could be made by observing the optical scattering produced by a search light [Synge, 1930]. Until this point, upper atmospheric soundings were performed primarily through the use of balloon observations. Balloon soundings above 50 km are not feasible, and the only alternative was the use of rockets [Synge, 1930]. In 1951, Elterman put Synge's idea to the test, and performed quantitative measurements of the stratospheric density with a searchlight [Elterman, 1951]. By using a shutter mechanism, Elterman was able to create a method for pulsing light that provided distinction between the transmitted and backscattered light which used a bistatic arrangement that pointed the receiving telescope along the beam to assign range values based on geometry. The concepts of using lasers to generate Raman scattering and the 'searchlight' technique are combined into current use of Raman lidars.

With the first demonstration of the laser in 1960, Theodore Maiman introduced a new tool for research to scientists around the world [Maiman, 1960]. Maiman's demonstration was the stimulated emission from a ruby crystal 1 cm in length and coated with silver on two parallel faces. Ruby absorbs the green, blue, and ultraviolet energy from a high-power flash-lamp and excites the ruby into a relatively long lifetime meta-stable state, which then decays as a red (694.3 nm) phosphorescent emission. The initial spontaneous emission spawns the stimulated emission of a powerful, nearly

monochromatic output at 694.3 nm along the axis established by the cavity gain; thus the laser was born.

Lasers have become well known and widely used in many areas because they provide a high-power controllable light transmitter. Lasers, which have a divergence of one milliradian or less, are significantly more collimated than the best search light (typically 0.1 radian divergence), and allow large power densities to be transmitted over longer ranges. In 1962, Smullin and Fiocco used a ruby laser to measure optical scattering from the moon, thereby demonstrating the capability of both the laser and detection optics of that time [Smullin and Fiocco, 1962]. Following their experiments using "moon echoes", they made measurements of scattering layers in the upper atmosphere [Smullin and Fiocco, 1963]. In 1964, Collis and Ligda performed backscattering measurements over the San Francisco Bay, where even during clear-sky conditions it was possible to distinguish areas aerosol scattering [Collis and Ligda, 1964]. The first work focused on elastic, or Rayleigh, scattering where the wavelength transmitted equals the wavelength received. Leonard performed the first lidar measurements of the Raman scattering from atmospheric molecular nitrogen and oxygen using a pulsed nitrogen laser at 337.1 nm, and analyzed the Raman scattered returns using a tunable filter with a bandwidth of 3.5 nm [Leonard, 1967]. This measurement was a great step forward because of the species' unique scattering wavelength; however, the Raman scattering-cross section is typically three orders of magnitude weaker than the Rayleigh-scattered component. A year later, measurements of atmospheric density with greatly improved accuracy were performed using the Raman return signal of nitrogen [Cooney, 1968].

By the early 1970s, the future of laser remote sensing measurements for the atmospheric monitoring of pollutants was developing. Inaba and Kobayasi [1970], Hirshfeld *et al.*, [1972] , Melfi and McCormick [1969, 1972] and Penney *et al.* [1974], had each performed their own experiments looking at water vapor, carbon dioxide, carbon monoxide, sulfur dioxide, and molecular nitrogen (N_2) and oxygen (O_2). Melfi and McCormick [1969] made measurements of water vapor by using a frequency-doubled ruby laser output from an ADP (ammonium di-hydrogen phosphate) crystal. By simultaneously measuring the atmospheric nitrogen and water vapor Raman signals, Melfi and McCormick obtained a measurement of the water vapor mixing ratio. Inaba and Kobayasi [1970] probed smoke plumes created by the burning of paraffin oil. With the smoke plume present, they identified the presence of both sulfur dioxide and carbon monoxide at a range of 20 m. Hirschfeld [1972] examined the means of improving the signal-to-noise ratio by taking advantage of the wavelength dependence of Raman scattering (λ^{-4}), as well as by using higher efficiency detectors and better filters for rejection of scattered signals from the fundamental laser wavelength. Hirschfeld [1972] was able to detect CO_2, SO_2, and water vapor at varying ranges and number densities in full daylight conditions. This work showed, for the first time, the experimental capability of Raman lidar to detect and quantify trace atmospheric pollutants in broad daylight. Penney *et al.*, [1974] made measurements of the absolute Raman scattering cross sections of N_2, O_2, and CO_2. In addition, they made observations of the temperature dependence of the rotational Raman scattering spectra, which today are used as a method to retrieve atmospheric temperature profiles.

Following these early experiments, many researchers [Poultney *et al.* 1977; Inaba 1976; and many others] continued to improve Raman lidar, making it possible to remotely detect a large array of chemicals and species in the atmosphere. Raman scattering provides a reliable ability to uniquely identify molecules. However, its very small scattering cross section decreases its utility with increased range and for small concentrations of the species. Therefore, in order to detect remotely small concentrations, it is necessary to find methods for increasing the signal. There are a number of ways to improve the detection of smaller quantities of chemical species with hardware improvements, or with other techniques such as fluorescence detection, Differential Absorption Lidar (DIAL), and resonance-enhanced Raman scattering.

We focus our efforts on the resonance-Raman technique that was demonstrated more than 60 years ago [Shorygin, 1947]. When the wavelength of optical excitation is tuned near an electronic absorption band, an increase in the Raman scattering efficiency is possible. Shorygin [1947] observed a resonance enhancement of Raman scattering through the use of mercury arc lamp radiation. Behringer and Brandmüller [1956] continued extensive studies of resonance Raman scattering into the mid 1950s. Laser developments in the early 1960s made it possible to probe molecular structures with a nearly monochromatic source, thus alleviating problems associated with wideband sources that mask Raman signals.

During the 1970s, Penney and Morey [1973] as well as Chamberlain *et al.* [1976], Rosen *et al.*, [1975] performed resonant Raman experiments on SO_2 and NO_2, and they demonstrated 3 to 5 orders of magnitude increase in Raman scattering compared with that of the background molecular nitrogen. These results pointed to the possibility of utilizing

Raman lidar as a means for detecting smaller concentrations of common air pollutants. Although the number densities of SO_2 and NO_2 were in the 1 to 100 ppm range, it was still feasible to detect them using the large increase in Raman scattering intensity from the resonant enhancement [Chamberlain *et al.*, 1975]. Hirschfeld *et al*. [1972] successfully detected SO_2 (30 ppm) in field experiments that examined plumes from smokestacks at a range of 200 m, and demonstrated this capability of the Raman lidar. Ziegler and Albrecht [1978] went on to perform the first measurements of the pre-resonant Raman scattering effects in benzene derivatives (e.g., benzene and toluene) and pioneered this work in organic chemistry. They followed that work with a resonance-enhanced Raman scatter measurements of benzene, utilizing the deep ultraviolet excitation at 212.8 nm (5^{th} harmonic Nd:YAG) [Ziegler and Albrecht, 1980]. Their research revealed strong resonant spectra with many combination modes and overtones present in the spectra.

Resonance fluorescence measurements of upper atmospheric sodium [Gardner *et al.*, 1988] were used to study the upper mesopause wave structure and temperature. The technique was extended to astronomy for atmospheric turbulence compensation by making use of the development of a solid state laser at 589 nm that coincided with electronic absorption of sodium [Philbrick *et al.*, 1985]. Clark and Dines [1986] made a comprehensive analysis of resonance Raman scattering and extended the work by detailing the theory of resonance-enhanced Raman scattering. Asher *et al.* [1993] used a new CW (continuous wave) laser source which —maintained hundreds of milliwatts of power in the deep UV at 257 nm, 248 nm, 244 nm, 238 nm and 228.9 nm— to study the resonance Raman process. This new CW laser source is ideal for Raman spectroscopy

because it avoids nonlinear and saturation problems that occur in materials when high peak intensity is used for excitation. By 1994, Sedlacek *et al.* [1994] created a resonance Raman lidar capable of detecting and measuring SO_2 pollutants in a plume at a range of 500 m, and demonstrated that it was possible to detect concentrations of 70 ppm·m with integration times as short as seven seconds.

With the development of several Raman lidars at Penn State University during the 1990s, a technique for measuring and analyzing ozone with sensitivity to a few parts per billion (ppb) level was developed [Esposito and Philbrick, 1998]. This high sensitivity resulted from using the Raman scattered signals of the fourth harmonic Nd:YAG laser (266 nm) from the atmospheric molecular nitrogen and oxygen, which coincidentally lie on the steep side of the Hartley absorption band in ozone. These signals provide a direct DIAL (Differential Absorption Lidar) measurement to retrieve profiles of ozone concentrations greater than about 10 parts per billion [Esposito and Philbrick, 1998]. This technique relies on the fact that the O_2-to-N_2 ratio in the atmosphere is stable to one part in 10^5, and only the absorption of ozone makes any substantial change in the measured ratio. Temperature measurements from 1 to 105 km have been demonstrated by combining Rayleigh and Raman scattering measurements in the lower region 1 to 80 km with resonance fluorescence of free metal atoms in the 80 to 105 km altitude region by using the Doppler width of the fluorescence returns [Alpers *et al.* 2004].

Resonance-enhanced Raman scattering is proposed as a likely solution to push the limits of remote detection for measuring minor atmospheric constituents or contaminants. When compared with classical Raman scattering in the visible, the resonance Raman

enhancements have shown increases in the scattered signals by several orders of magnitude [Chamberlain *et al*., 1976].

Chapter 3:
Optical Scattering

Optical scattering is responsible for many atmospheric phenomena. As light waves propagate through the atmosphere, they scatter off of the molecules in the air. The most well-known effect is the blue sky, which is due to atmospheric molecular scattering, often referred to as Rayleigh scattering. Most of the photons incident on molecules are elastically scattered and the cross section is proportional to λ^{-4}. One might then argue that the sky should be purple, but the solar spectrum is peaked at yellow wavelengths, and the human eye is also more responsive to blue than purple; therefore, the scattered light in the eye's photometric response appears blue. There are many other phenomena that result from optical scattering, such as a rainbow, which is produced by the refractive dispersion of light at the air-water interface of the nearly spherical water droplets, as seen in Figure 3.1. Figure 3.2 shows a sundog that is the result of refraction at the surface of small ice crystals in the air. The phenomenon known as the green flash, which results from the fact that shorter wavelengths scatter through larger angles than do the longer wavelengths, is shown in Figure 3.2. As the Sun sets, the red end of the spectrum no longer bends enough to be seen above the horizon, and then the green and blue portions of the spectrum are left to create a flash of green light for a brief moment of time the green intensity is larger than blue. Each of these phenomena is a result of light scattering from particles, without any change in energy or wavelength of the scattered photon. A far less probable form of light scattering, and one more difficult to observe, was discovered

by C.V. Raman, and thus has become known as Raman scattering. Raman scattering occurs when there is a difference in incident and scattered energy that involves the exchange of energy between the incident photon and the energy states of a molecule, and therefore results in a significant difference between the incident and scattered wavelengths.

Figure 3.1. Rainbow (contributed by David Willitsford)

Figure 3.2. Left: Sundog (New Ulm, MN, Erik Axdahl)

Right: Green flash (San Francisco, CA, Mila Zinkova)

3.1 C.V. Raman and Raman Scattering

Raman scattering has been developed into a standard laboratory technique since its discovery in 1928 by C.V. Raman [Raman, 1928]. Because there was such a great interest in the newly discovered phenomenon by the end of 1928, the year of the discovery, 70 publications were in print. The following year saw continued growth in this research topic with more than 200 papers published. By the end of the 1930s more than 1800, papers documenting the spectra of over 2500 samples, had been published [Fabelnskii, 1998].

Appendix A shows the first photograph of the molecular vibration spectra taken by C.V. Raman. This discovery was so profound and useful to the advancement of science, that in 1930 Raman was awarded the Nobel Prize for his efforts in optical scattering [Nobel Prize, 1930]. Raman scattering is a process by which light scatters from a molecule at a different wavelength or energy than that which was incident on the molecule. The change in wavelength of the scattering photon results from energy exchange with the molecules' energy states, including vibration, bending, stretching, or rotational transitions. Early studies using Raman spectroscopy provided much data on the vibrational energy states and spectra of many molecules [Hibben, 1939]. The vibrational spectrum provides the traditional 'fingerprint' that is used in the identification of molecules from their infrared absorption and/or Raman scattering. Because the vibrational states of a molecule are determined by the mass of the atoms as well as their bond strengths and bond angles, the quantized modes are unique for each molecule. By exciting these different vibrational and rotational modes and then analyzing the resultant Raman scattered

spectra, one can use Raman spectroscopy as a powerful tool for uniquely locating, identifying, and quantifying unknown molecular species.

3.1.1 Stokes and Anti-Stokes Raman Scattering

Raman scattering is subdivided into Stokes and anti-Stokes Raman scattering components. A Stokes shift results when the scattered radiation appears at a lower energy, or a longer wavelength (red-shifted), relative to the incident radiation, and anti-Stokes scattering results when the scattered radiation occurs at a higher energy, or shorter wavelength (blue-shifted). Figure 3.3 illustrates a virtual energy diagram showing the difference between Rayleigh scattering, Stokes scattering and anti-Stokes scattering. In the diagram ν_0, is the ground state, ν_e is the vibrationally excited state, and $\Delta\nu$ is the energy of the scattered photon. Rayleigh scattering results when the initial and final state of the molecule is the same, and no loss or gain of energy occurs. Stokes Raman occurs when the molecule keeps some of the incident energy and scatters a photon with lower energy, red-shifting the scattered light. Anti-Stokes Raman occurs when the molecule starts in an excited state and the donates energy to the scattered photon, blue-shifting the scattered light.

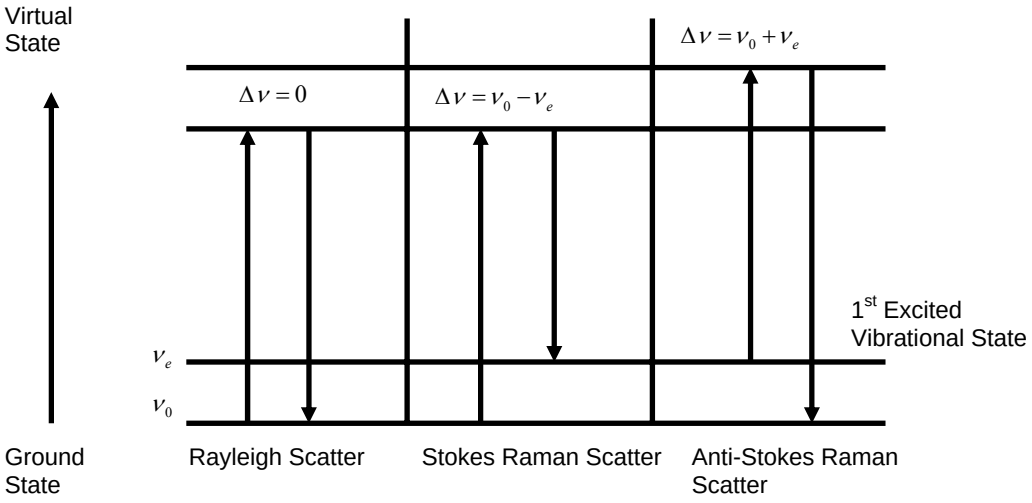

Figure 3.3. Optical scattering, ν_0 is the ground state, ν_e is the vibrationally excited state, and $\Delta\nu$ is the energy of the scattered photon [Inaba, 1976]

The Stokes Raman scattering is more probable because most molecules are in their ground state; however, with increasing temperature more of the molecules will be elevated to an excited state, as predicted by the Boltzmann distribution,

$$f(E) = Ae^{-\frac{E}{kT}},$$

where the probability that a molecule will have energy, E, depends on its temperature T, and a normalization constant, A. With increasing temperature, the Boltzmann distribution results in a higher probability that the molecule will reside in an excited state, and so scattering may result in an anti-Stokes component. Because Raman scattering is dependent on the initial state of the molecule, it is possible to retrieve the temperature by taking the ratio of the Stokes to anti-Stokes Raman signals [Alpers *et al.*, 2004]. The changes in the probability distribution function of the rotational states will also yield in the rotational Raman scattered signals that permit calculations of the temperature.

3.1.2 Vibrational Raman Spectral 'Fingerprints'

Raman scatter depends on the initial state of the molecule and on the set of quantized energy states associated with the vibration, rotation, stretching, and bending of the molecules bonds, which determine the spectral fingerprint. Each molecule has a unique structure, mass, bond length, and bond strength, and therefore maintains its own set of unique Raman shifts associated with the quantized energy levels of each dynamical mode of a molecule. Using the molecule's physical characteristics, the energy shift associated with the vibrational or rotational transitions within the simple molecules can be calculated. The energy shifts associated with the quantized transitions can be imparted to the molecule and thereby subtract from the incident energy in the case of Stokes scattering (red-shift). Alternatively, the energy of a vibration (or rotation) may be released or added to the incident energy when the molecule resides in an energy state above the ground state, and this process is referred to as anti-Stokes scattering (blue-shift). Figure 3.4 displays the vibrational shift for an array of molecules. It should be noted that the largest shift, 4160 cm^{-1} (wavenumbers) is associated with H_2 because the hydrogen bond is the strongest, thus exchanging the most excitation energy. Because hydrogen has the strongest bond that can participate in Raman scattering, the bandwidth is typically taken to be ~4200 cm^{-1} and corresponds to the 2.4 μm end of the optical spectrum. Thus, any Raman scattered light (excluding multiple phonons, combination modes, or overtones) will occur within 4200 cm^{-1} of the excitation wavenumber. Appendix B shows typical Raman scattering energies for different vibrational groups.

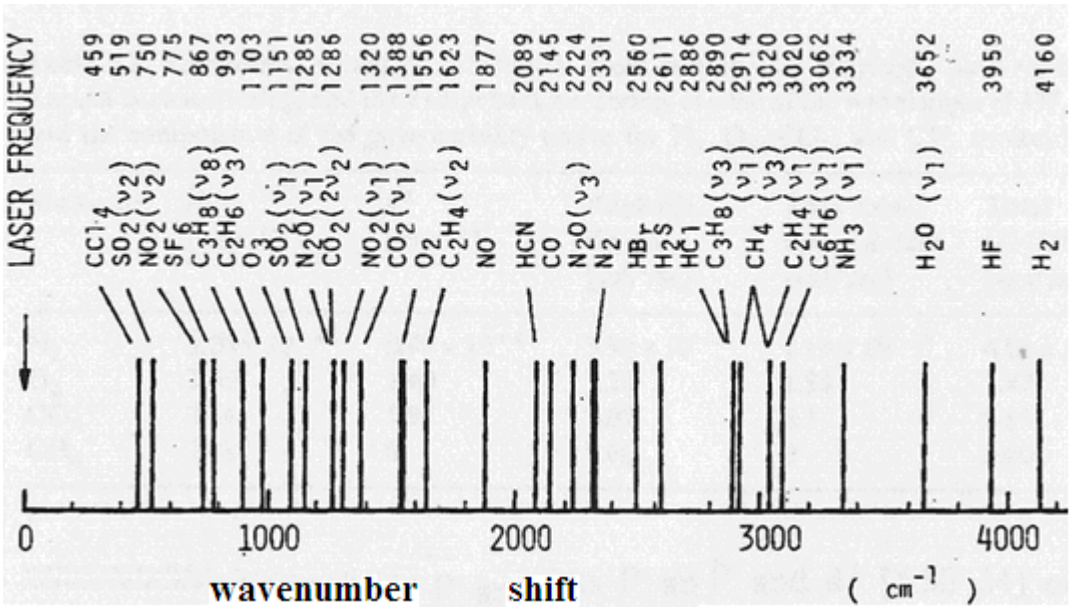

Figure 3.4. Vibrational Raman shift of a collection of molecules [Inaba 1976]

The energy shifts noted above are part of the vibrational spectral fingerprint of the molecules. The spectrum of the scattered radiation provides an easy method to distinguish the different molecules, because the scattered wavelength is Raman-shifted by a vibrational energy level specific to each molecules properties. For example is a laser beam from the 2nd harmonic of the Nd:YAG laser is Raman scattered by hydrogen,

$$\text{Incident Wavelength} = 532\ \text{nm}\ \ (2\text{nd Harmonic Nd : YAG Laser})$$
$$H_2\ \text{RamanShift} = 4160\ \text{cm}^{-1}$$
$$18797\,\text{cm}^{-1} - 4160\ \text{cm}^{-1} = 14637\ \text{cm}^{-1}$$
$$\frac{14637}{\text{cm}} * \frac{100\ \text{cm}}{1\ \text{m}} = 2403280\ \text{m}^{-1}, \text{ corresponding to } 683.2\,\text{nm}.$$

The first vibrational shift for H_2 occurs at 4160 cm^{-1}. When hydrogen is excited by a laser at a wavelength of 532 nm, this excitation wavelength will result in a vibrationally scattered wavelength of ~ 683.2 nm. With the detection of scattered radiation at 683.2 nm, the presence of hydrogen is confirmed. The magnitude of the

signal may also be used to make calculations of the quantity of hydrogen present. With shorter excitation wavelengths, the Raman scattered spectra spanning ~ 4000 cm^{-1} becomes compressed to the wavelengths shown in Table 3.1 for excitation at 250 nm and 500 nm.

Table 3.1. Raman Spectral Range

Excitation Wavelength	4000 cm^{-1}	$\Delta\lambda$
250 nm	277.8 nm	27.8 nm
500 nm	625 nm	125 nm

3.1.3 Rotational Raman Scattering

Energy shifts associated with rotational modes of a molecule are significantly smaller in energy than are the vibrational modes. Typical rotational Raman shifts are in the range from 5 cm^{-1} to 200 cm^{-1}, and the rotational spectral lines thus appear close to the Rayleigh (elastically) scattered line [Penney, 1974]. Figure 3.5 shows a Morse potential diagram depicting the energy levels of a typical atom or molecule. The ν levels represent the vibrational states of the molecule, and the *R*-levels represent the rotational states of the molecule, with ν_0 being the rest state.

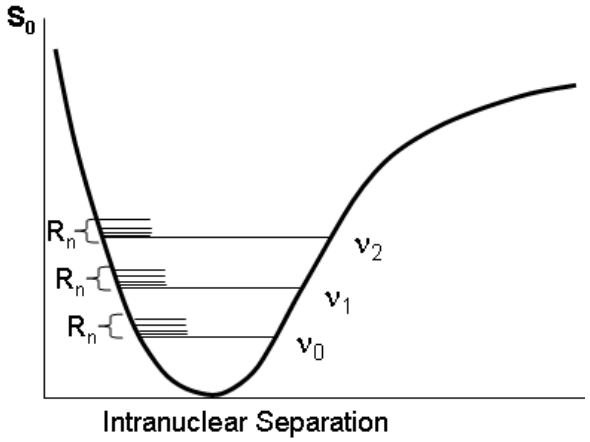

Figure 3.5. Vibrational and rotational energy diagram, ν levels correspond to vibrational states and R_n levels correspond to rotational states

It is relatively straight-forward to model and calculate the rotational Raman scatter of simple two-atom rotors, which typically represent the atmospheric molecules, nitrogen (N_2) and oxygen (O_2) [Behrendt and Nakamura, 2002]. The rotational lines occur on both the Stokes and anti-Stokes sides of the incident radiation; the Stokes features will have larger cross-sections, because of the larger probability that the molecules reside in lower energy states. Figure 3.6 shows the calculated rotational Raman spectra for a simple two-atom rotor such as nitrogen and oxygen at 200 K. For comparison, Figure 3.7 shows the rotational Raman spectra for nitrogen and oxygen at 300 K; notice that rotational states further from the center (Rayleigh line) are populated as the higher temperature broadens the distribution, also notice that the populations of the lowest energy states —those closer to the Rayleigh line— decrease as the higher states are populated. There is also a change in the magnitude of each state, as more of the energy is coupled into the higher energy states.

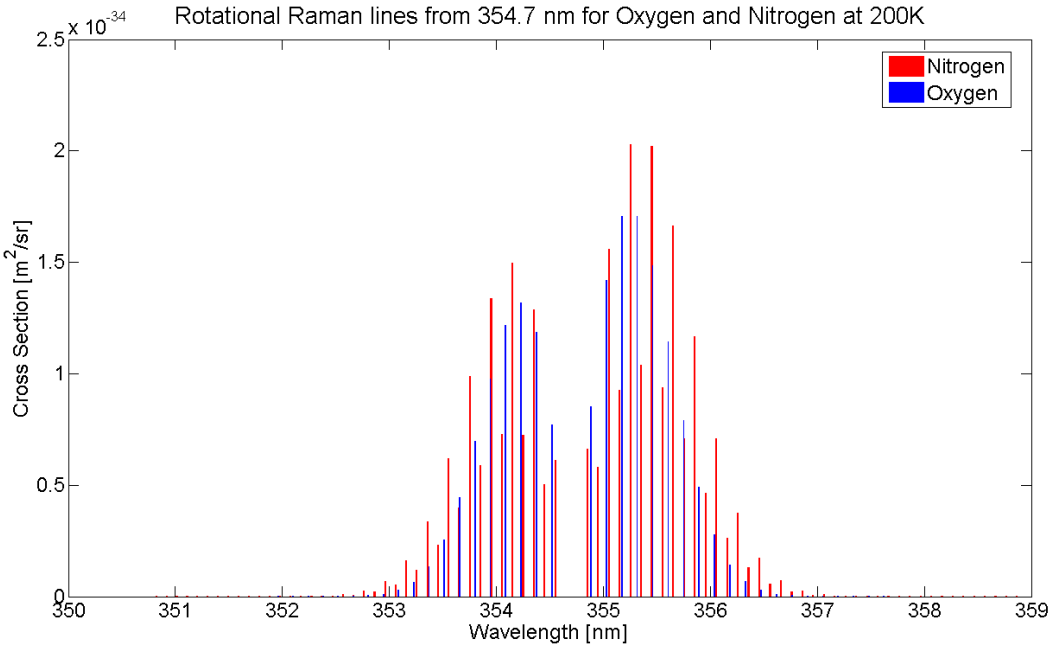

Figure 3.6. Rotational Raman lines for oxygen and nitrogen at 200K

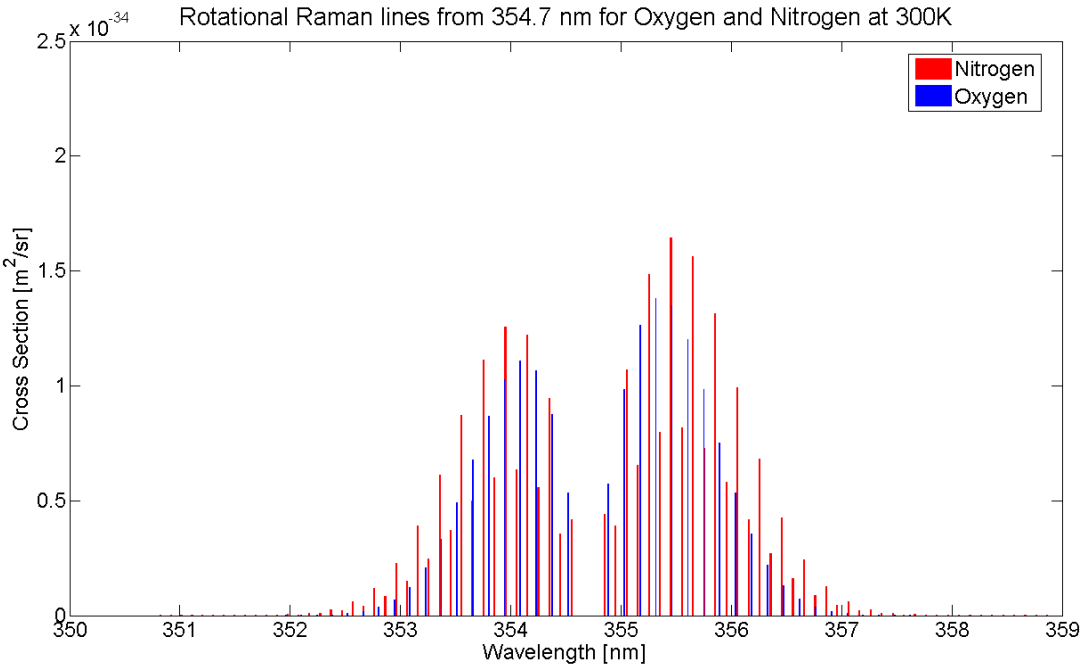

Figure 3.7. Rotational Raman lines for oxygen and nitrogen at 300K

3.2 Coherent Anti-Stokes Raman Spectroscopy

Coherent anti-Stokes Raman scattering, or CARS, is a nonlinear optical process typically described as four-wave mixing [Tolles *et al.*, 1977]. Coherent Raman spectroscopy yields similar information to normal Raman scattering; due to the efficient transfer of energy to the scattering medium however, signal levels may be improved by as much as nine orders of magnitude [Melveger, 1978]. CARS is a useful tool for probing chemicals in a laboratory situation, but there are several obstacles when applying this technique to remote sensing. The coherent anti-Stokes Raman scatter is exclusively a forward-scatter process, meaning that a traditional Raman lidar that relies on back-scattered signals would not be possible. Also, in order for the coherent Raman scattering process to occur, the pump and probe beams must be perfectly overlapped, both spatially and temporally.

3.2.1 Pump, Probe, and Four-wave Mixing

The coherent process known as four-wave mixing involves the interaction of three electromagnetic fields to create a fourth field, in this case it is the anti-Stokes Raman scatter. The process of electromagnetic interaction with a material can be expanded using a Taylor series of the induced polarization $\vec{P}$, in terms of the applied local electric field,

$$\vec{P} = \varepsilon_0 \chi^{(1)} \vec{E} + \varepsilon_0 \chi^{(2)} \vec{E}^2 + \varepsilon_0 \chi^{(3)} \vec{E}^3 + \ldots,$$

where $\chi^{(1)}$ is known as the linear electro-optic effect or Pockels effect. The Pockels effect is used in Pockels cells to provide a linear voltage-controlled optical polarization rotator. The $\chi^{(2)}$ effect is known as the quadratic electro-optic effect or Kerr Effect. Although the Kerr effect is typically weaker than the Pockels effect, it was discovered first in 1875, because it is present in all materials. In contrast, the Pockels effect was only discovered in 1893, because it is only found in noncentrosymmetric materials. The study of CARS involves utilizing the $\chi^{(3)}$ effect, in which three electromagnetic fields interact to form sum and difference frequencies coherently to generate an anti-Stokes photon. Although there are only two different beams, the process is still considered to be four-wave mixing as the incident radiation is degenerate and is used twice during the coherent Raman process. Figure 3.8 shows the CARS process that generates the anti-Stokes signal. In the CARS process,

$$\upsilon_c = 2\upsilon_p - \upsilon_s ,$$

where

ν_p is the incident (pump) radiation energy,
ν_s is the Stokes (probe) radiation energy,
ν_c is the scattered radiation or CARS signal energy.

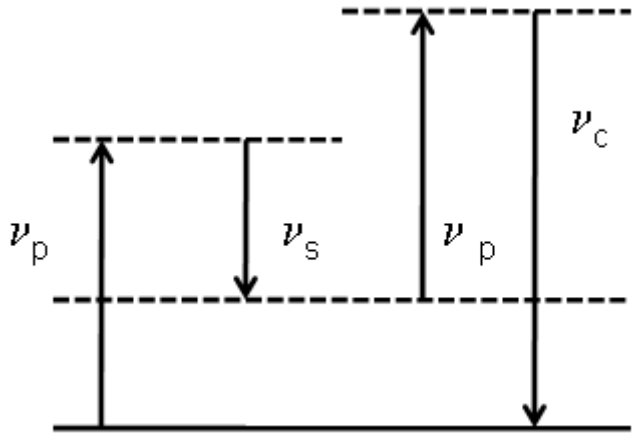

Figure 3.8. Coherent anti-Stokes Raman spectroscopy. Two pump photons ν_p are mixed with the stokes photon ν_s to retrieve the scattered photon ν_s

When the difference between ν_p and ν_s is equal to a vibronic energy level, a resonant enhancement is seen in the CARS signal.

$$\upsilon_r = \upsilon_p - \upsilon_s \quad \text{(resonant enhancement)}$$

The resonant enhancement will occur when this relation is satisfied, thus increasing the CARS signal by several orders of magnitude.

3.2.2 White Light Laser (Stokes Probe)

As is mentioned above, in order to see the large signal increase associated with scanning CARS, it is necessary to scan the Stokes (probe) laser beam. However, by utilizing a supercontinuum "white light" laser there is no need to scan the probe because the laser energy is already present in each pulse. A white light laser is an extremely broadband laser source that is spatially coherent but temporally incoherent.

Spatial coherence means that it is possible to focus and collimate the laser beam, while temporal incoherence means that it has a broadband emission. It is commonly called a white light laser because the laser is white due to the presence of laser light throughout the visible spectrum.† By utilizing an ultra-fast laser pulse (~femtosecond) propagated through a highly nonlinear fiber, it is possible to generate a laser beam with a supercontinuum spectrum. Figure 3.9 shows a prism expansion of a supercontinuum white light laser developed in the Ultra-fast Optics Lab at The Pennsylvania State University.

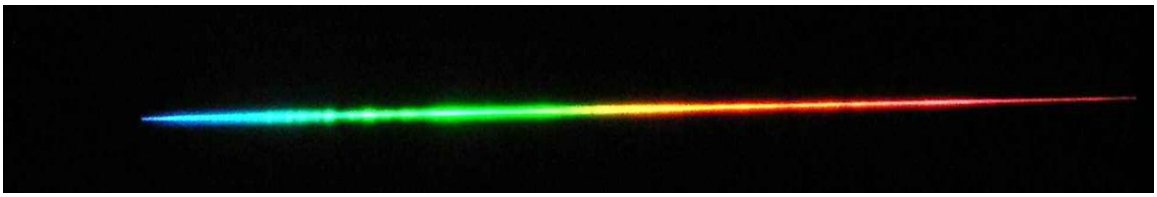

Figure 3.9. Dispersion of the supercontinuum white light laser in the Ultra-fast Optics Lab at Penn State University

3.3 Fluorescence

Fluorescence is a serious obstacle in Raman scattering studies because even low levels of photoemission can mask the much weaker Raman effect. The fluorescence cross section can exceed the Raman scattering cross sections by as many as 12 orders of magnitude [Inaba, 1978]. Fluorescence is the spontaneous emission of a photon following excitation of electronic states by the absorption of incident radiation. Non-radiative transitions following the absorption result in spontaneous re-emission in a band of wavelengths and often create a broadband emission (fluorescence), which can mask the Raman return. The schematic Figure 3.10

† Supercontinuum is more commonly accepted because it applies to any broadband laser source, either in the ultraviolet, visible, or infrared without the need for an actual beam to appear white.

represents the mechanism by which broadband emission occurs, when creating the fluorescent effect. The fluorescent process in many molecules experiences a *quenching* effect in the lower atmosphere, where the scattering intensity is lowered by several orders of magnitude due to collisions that dissipate energy without the emission of a photon. In a low-pressure situation either in a laboratory chamber or in the upper atmosphere (where collisions are less frequent), this quenching effect is greatly reduced. Although the quenching effects reduce the intensity of fluorescence, the signal may still be too strong to distinguish any underlying Raman scattered light.

Other means of reducing fluorescence and other unwanted signals, must be employed to measure the weaker Raman scattered signals. A common method of reducing background signals is accomplished by the use of narrowband filters centered on the wavelength of the expected Raman scattered signals. Another method for reducing the interference of fluorescence is through the use of time gating of the scattered signals for pulsed laser excitation [Matousek, 2000]. Raman scattering is nearly instantaneous; however, the broadband process of fluorescence is much slower and can be partially separated by preventing the detector from counting photons beyond the interval corresponding to immediate scattering of the fundamental laser pulse.

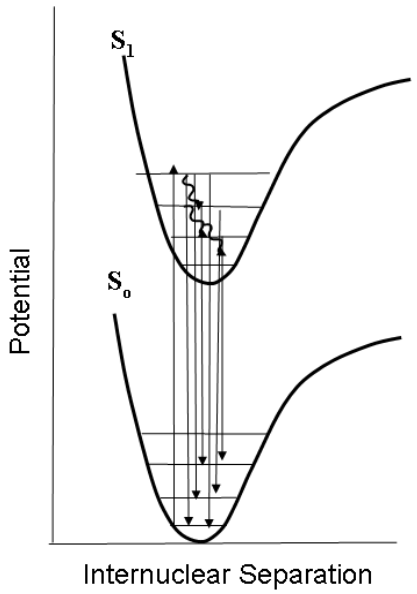

Figure 3.10. Broadband emission due to fluorescence, S_o is the ground state and S_1 is the excited state

3.4 Resonance Raman Scattering

Resonance Raman scattering occurs when the wavelength of excitation falls near or within an electronic or vibrational absorption band of the molecule, and thereby enhances the coupling of energy into the vibrational modes of the absorbing species. This scattering enhancement can be as much as 3-to-8 orders of magnitude larger than that of classical Raman scattering [*Chamberlain et al.*, 1976]. Although the resonance effect greatly enhances the scattering power, this effect is not always observed easily because the simultaneous higher absorption, combined with the interfering effects of fluorescence, may hide the enhanced Raman scattered radiation. Figure 3.11 shows a comparison of Raman scattering, pre-resonance Raman, resonance Raman, and fluorescence interactions. The upward portion of the arrows represents the incident energy with the curved peak being the point where the scattering results and the downward portion of the arrow represents the Raman

scattered wavelength. The approximate scattering cross sections for each of the different scattering mechanisms are listed in Table 3.2.

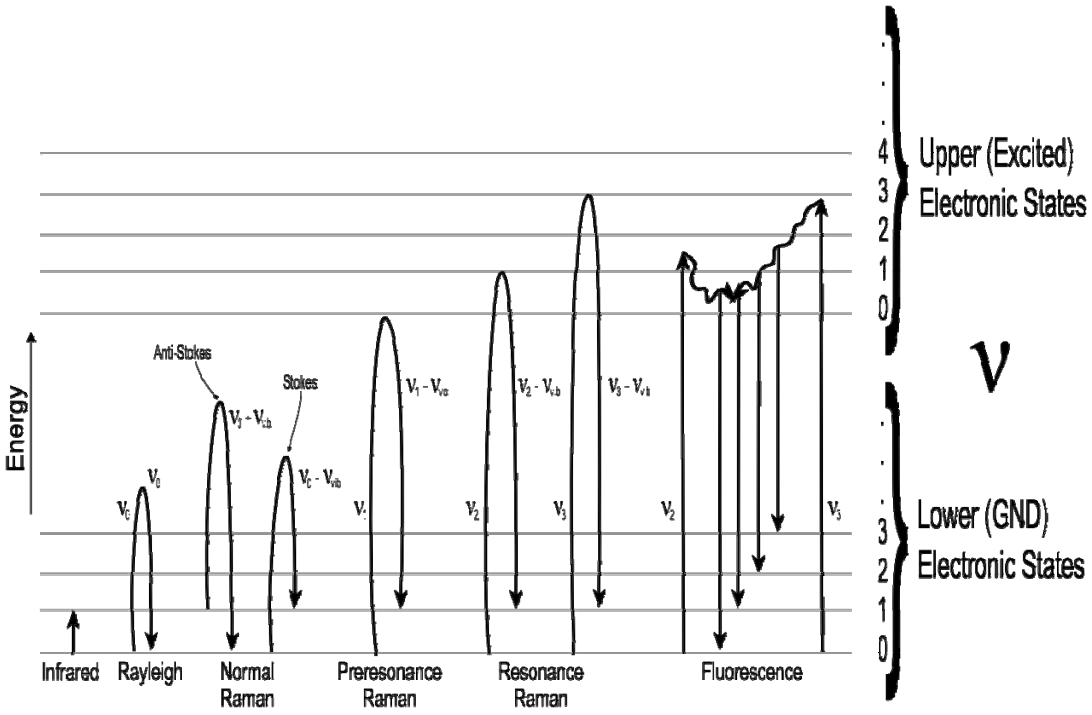

Figure 3.11. Optical scattering mechanisms [Inaba, 1975]

The fluorescent signal may be quite large and is also very broad, resulting in little opportunity to identify it due to its broadband emission. Fluorescence occurs in many different chemical and biological molecules, however, its specificity is lost due to the non-radiative transitions occurring in the scattering medium. As a result, it is often possible to use fluorescence as a means for detection of a broad class of materials, but not as a means to identify a specific material. The fluorescent emission is very slow relative to Raman scattering, and allows the vibrational energy of the electronic states to degenerate back to its lower vibrational levels. Therefore, the wavelengths of the fluorescence photons are mostly independent of the incident

radiation; thus the Raman signals do reflect the energy states unique to the scattering molecules [Levenson, 1989]. Most molecules do not generally fluoresce with any significant intensity when the excitation energies are below about 280 nm, and this factor can be very important for investigations of the resonance Raman properties.

Table 3.2. Optical scattering cross sections [Inaba, 1975]

Interaction	Process	Frequency Relation	Cross-Section $(\frac{cm^2}{sr})$	Detectable Constituents
Scattering	Mie	$\nu_r = \nu_0$	$10^{-26} - 10^{-8}$	Particulate Matter
	Rayleigh	$\nu_r = \nu_0$	10^{-26} (NR)	Atoms & Molecules
			10^{-23} (R)	
	Raman	$\nu_r \neq \nu_0$	10^{-29} (NR)	Molecules (atoms)
			10^{-26} (R)	
Emission	Fluorescence	$\nu_r = \nu_0$	10^{-26} (Quenched)	Atoms & Molecules
		$\nu_r \neq \nu_0$	10^{-24} (Quenched)	
Absorption		$\nu_r = \nu_0$	10^{-20}	Atoms & Molecules

ν_r: Detection Frequency, ν_0: Laser Frequency; NR: Non-Resonance, R: Resonance, (*Inaba*)

3.5 Lidar

Lidar (Light Detection And Ranging), commonly referred to as laser radar, has been developed as a method of remotely detecting several of the chemical species in the atmosphere. The Penn State Lidar Lab has developed a number of Raman lidar instruments, and used them for the investigations of the properties and processes in the atmosphere. The focus of recent studies has been on the investigations of atmospheric properties, and molecular species [Brown *et al.*, 2008, Philbrick *et al.,* 2006. Willitsford *et al.* 2005].

3.5.1 Lidar Fundamentals

A lidar system transmits a pulsed laser beam into the atmosphere where it is scattered from molecules and aerosols. The molecules in the atmosphere —primarily nitrogen (N_2), oxygen (O_2) and water vapor (H_2O)— scatter the energy from a laser beam, this scattered energy is collected and analyzed. A monostatic lidar transmits and receives on the same axis, while bistatic or multistatic receivers are located off of the transmit axis to provide information on the angle dependence of the scattered radiation. In either setup, the scattered signals are generally measured with a photomultiplier tube (PMT) in analog or digital counting mode, or with a solid state detector. The collected signals are then analyzed to obtain results on the concentration of atmospheric constituents, or to determine one of several meteorological properties. The backscattered return signals contain information from both Rayleigh and Raman scattering processes. The rotational Raman scattered signals carry the specific information on atmospheric temperature, and the vibrational scattered signals contain information on the concentration of molecular species, such as water vapor and ozone.

3.5.2 LAPS

The LAPS (Lidar Atmospheric Profile Sensor) instrument, shown in Figure 3.12, was developed at Penn State by faculty, staff, and graduate students as an operational prototype for the United States Navy. The LAPS unit was initially constructed to measure atmospheric temperature and water vapor profiles to support meteorological forecasting, to correct radar returns affected by RF refraction, and to

demonstrate a replacement for cumbersome radiosonde[‡] measurements. The LAPS unit was successfully tested in September and October of 1996 in the Gulf of Mexico and the Atlantic Ocean [Philbrick, 1996]. Following these tests, the LAPS unit has been used as a research tool for investigating and characterizing the evolution of air pollution episodes. The LAPS lidar has proven its utility with extensive studies of atmospheric water vapor, temperature, ozone, and particulates [Philbrick *et al.* 1997, Esposito and Philbrick, 1998; Philbrick and Mulik, 2000.]. The data collected by the LAPS Raman lidar have been supplemented with balloon sonde measurements as well as aircraft measurements to develop a more complete picture of complex atmospheric interactions [Philbrick *et al.,* 2003].

[‡] A radiosonde or balloon sonde is a meteorological sensor package attached to a helium-filled balloon. It is released into the air and during its ascent transmits measurements of atmospheric properties back to a base station on the ground.

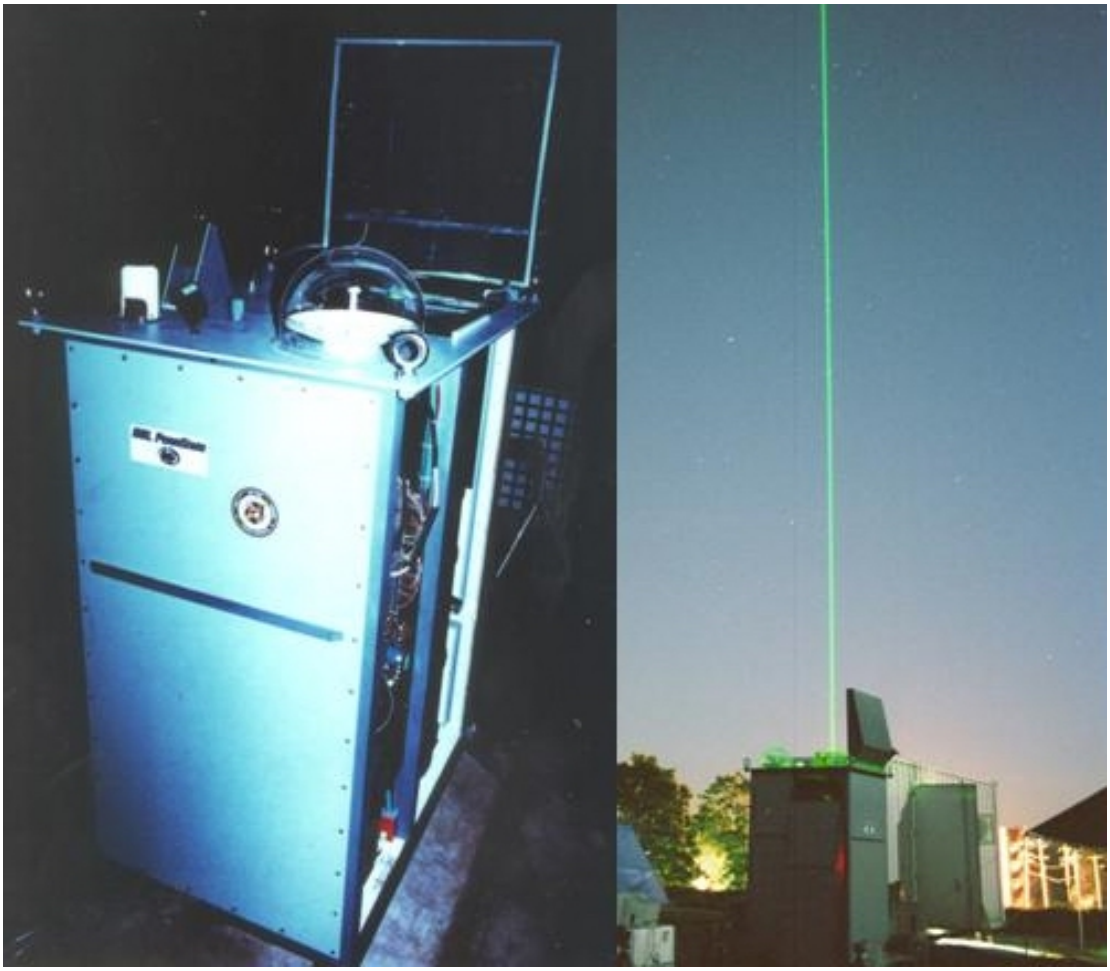

Figure 3.12. Lidar Atmospheric Profile Sensor (LAPS) at Penn State University

3.6 Summary

Rayleigh scattering where the scattered wavelength is essentially the same as the incident wavelength, in the natural atmosphere is a commonly observed phenomenon. A far less probable form of optical scattering is known as Raman scattering. Raman scattering from incident laser beams has proven to be a useful tool for the identification and quantification of many molecules. Following the developments of the laser in the early 1960s that provided a coherent and nearly monochromatic source, Raman scattering using laser beams has proved to be most valuable in locating and identifying unknown chemical species. The extremely small

scattering cross section of non-resonant Raman scattering make it difficult to detect, identify, and quantify small concentrations of chemical species. Lidar measurements of molecular concentrations are possible when using backscattered signals from the unique fingerprints of Raman spectra. By using the resonant enhancement process, a further extension of Raman spectral analysis is possible. Resonance-enhanced Raman scatter is expected to extend lidar remote sensing techniques by improving signal-to-noise ratio and permitting detection of lower concentrations of molecular species over larger distances.

Chapter 4: Theory of Resonance-Enhanced Raman Scattering

An overview of the theoretical background of resonantly enhanced Raman scattering is now provided as a foundation for this subject. The theory was first developed by Shorygin [1947] and expanded by the work of Albrecht [1961]. Over the years, many different methods for presenting and interpreting the theory of resonant enhanced Raman scatter have been proposed [Albrecht, 1961; Behringer, 1974; Spiro, 1977; Hong, 1977a and 1977b]. I have chosen to present a summary based upon the work of Clark and Dines [1986], with additional contributions of Long [2001]. The results and equations from this approach have become widely used and well-known within the community of researchers who work in the field.

4.1 Classical Light Scattering – Dipole Scattering

Raman scattering occurs when a dipole is induced in a molecule by the electric field of the applied electro-magnetic wave, and the result is dipole scattering from the molecule. The time-averaged power per unit solid angle is [Long, 2001],

$$I = k_{\nu}' \nu_s^4 p_o^2 \sin^2(\theta), \qquad [4.1]$$

where,

$$k_{\nu}' = \frac{\pi^2 c_0}{2\varepsilon_0},$$

p_0 is the amplitude of the induced dipole of frequency ν_s (scattered), and

θ is the angle with respect to the axis of the dipole.

The induced electric dipole can be viewed as a sum of an infinite series

$$p_o = p^{(1)} + p^{(2)} + p^{(3)} + \ldots,$$

which generally converges quite quickly [Long, 2001] because

$$p^{(1)} >> p^{(2)} >> p^{(3)}$$

$\vec{p}^{(1)} = \alpha\vec{E}$ where α is the molecular polarizability tensor of 2nd rank,

$\vec{p}^{(2)} = \frac{1}{2}\beta\vec{E}\vec{E}$ where β is the hyperpolarizability tensor of 3rd rank,

$\vec{p}^{(3)} = \frac{1}{6}\gamma\vec{E}\vec{E}\vec{E}$ where γ is the second hyperpolarizability tensor of 4th rank.

By substituting p_0 into Equation [4.1], one retrieves [Long, 2001],

$$I = k_\nu' \nu_s^4 \left[\alpha\vec{E}(\nu_{laser})\right]^2 \sin^2[\theta]. \qquad [4.2]$$

From Equation 4.2, it is clear that the intensity of the scattered light is proportional to the fourth power of the scattered frequency and to the square of the E-field strength.

4.1.1 Rayleigh and Raman Scatter

By utilizing a Taylor series expansion and ignoring higher terms the polarizability tensor α can be described [Long, 2001] as,

$$(\alpha_{\rho\sigma})_k = (\alpha_{\rho\sigma})_0 + \left(\frac{\partial\alpha_{\rho\sigma}}{\partial Q_k}\right)_0 Q_k, \qquad [4.3]$$

where,

$$Q_k = Q_{k0}\cos(\nu_k t + \delta_k).$$

Therefore, the polarizability tensor at frequency ν_k is equal to the polarizability tensor at the equilibrium point plus a perturbation from the equilibrium point that depends on ν_k. The electric field from the incident radiation field is,

$$\vec{E} = \vec{E}_0 \cos(\nu_l t),$$

where ν_l is the frequency of excitation (laser).

Examining $\vec{p}^{(1)} = (\alpha_{\rho\sigma})_k \vec{E}$, we can then calculate the time dependence of the induced electric dipole from the E-field and the polarizability tensor [Long, 2001], i.e.,

$$\vec{p}^{(1)} = (\alpha_{\rho\sigma})_0 \vec{E}_0 \cos(\nu_l t) + \left(\frac{\partial \alpha_{\rho\sigma}}{\partial Q_k}\right)_0 Q_{k0} \cos(\nu_k t + \delta_k) \vec{E}_0 \cos(\nu_l t).$$

By applying the trigonometric identity,

$$\cos(a)\cos(b) = \frac{1}{2}[\cos(a-b) + \cos(a+b)],$$

it is possible to separate the frequency components of the induced dipole moment into an elastically scattered component, as well as the Raman Stokes and anti-Stokes components.

When the molecule of interest is excited by the incident electric field, a dipole moment is created that oscillates at the excitation frequency and thereby re-radiates energy at the same frequency resulting in elastic or Rayleigh scatter. In the same volume, a small fraction of the molecules becomes excited and modulates the incident frequency by ($\pm\ \nu_k$) creating Raman Stokes and Raman anti-Stokes features which can be described as,

$$\vec{p}^{(1)} = \underbrace{\left(\alpha_{\rho\sigma}\right)_0 \vec{E}_0 \cos\left(\nu_l t\right)}_{\text{Rayleigh}} + \underbrace{\left(\frac{\partial \alpha_{\rho\sigma}}{\partial Q_k}\right)_0 Q_{k0} \cos\left(\nu_k t + \delta_k\right) \vec{E}_0 \cos\left(\nu_l t\right)}_{\cos(a)\cos(b) = \frac{1}{2}\left[\cos(a-b) + \cos(a+b)\right]}$$

$$\text{Raman}$$

$$\left(\frac{\partial \alpha_{\rho\sigma}}{\partial Q_k}\right)_0 Q_{k0} \vec{E}_0 \frac{1}{2}\left[\cos\left(\nu_l t - \nu_k t\right) + \cos\left(\nu_l t + \nu_k t\right)\right]$$

Stokes Anti-Stokes

hence,

$$p^{(1)}_{\text{Rayleigh}}\left(\nu_l\right) = \left(\alpha_{\rho\sigma}\right)_0 \vec{E}_0 \cos\left(\nu_l t\right)$$

$$\vec{p}^{(1)}_{\text{Raman}}\left(\nu_k + \nu_l\right) = \left(\frac{\partial \alpha_{\rho\sigma}}{\partial Q_k}\right)_0 Q_{k0} \vec{E}_0 \frac{1}{2}\left[\cos\left(\nu_l t - \nu_k t\right) + \cos\left(\nu_l t + \nu_k t\right)\right].$$

Because all molecules are polarizable [Long, 2001], a portion of α_0 will be non-zero and, therefore, Rayleigh scattering will always exist. In order for Raman scattering to occur (i.e. Raman active), the polarizability must change so that,

$$\left(\frac{\partial \alpha_{\rho\sigma}}{\partial Q_k}\right)_0 \neq 0 .$$

That is, the derivative of the polarizability with respect to the normal mode must be non-zero in the case of Raman scattering. It follows that if there is no change in the polarizability due to an induced dipole moment, then the polarization of the scattering wave, $\vec{p}^{(1)}_{\text{Raman}}\left(\nu_k + \nu_l\right)$ will be zero. In this case, there will be no resultant scattering at either the Stokes or anti-Stokes Raman wavelengths.

4.2 Infrared Active and Raman Active Selection Rules

In order for a molecule to be infrared active so that infrared absorption at a certain frequency is allowed, the molecule must first have a permanent electric dipole moment. This dipole moment can then be modulated at the incident frequency, thus it is infrared active and absorbs energy from photons with energies near the energy of resonance corresponding to its quantized energy state. In order for a molecule to be Raman active so that a certain mode can be excited, a dipole moment must be induced by the electric field of the incident radiation. This induced dipole moment is a result of the motions of the electrons relative to the nucleus caused by the electric field of the scattering photon. Finally, the rule of mutual exclusion states that, if a molecule has a center of symmetry, then there are no modes that are both infrared and Raman active [Long, 2001].

4.3 Dirac Notation - Bra-Ket Operators

In order for the quantum mechanical equations to describe the absorption and scattering processes, we choose to use the notation for quantum states that was first introduced by Paul Dirac [Dirac, 1939] called bra-ket, from the "bra" and "ket" in "bracket". The 'left' quantum state is defined as the bra $\langle a|$, and the 'right' quantum state is the ket $|b\rangle$. When combined $\langle a|b\rangle$, the bra-ket operator represents the inner product of *a* and *b*. In the case of quantum states, the complex conjugate is implied in the bra operator, but not in the ket. That is we have,

$$\Psi^* = \langle \Psi |.$$

The combination of the bra-ket operator is most commonly used as a multiple integral,

$$\int \Psi^* \Psi dQ_1 = \langle \Psi | \Psi \rangle,$$

and, more specifically,

$$\langle a | A | b \rangle = \int \Psi_a^*(x) A \Psi_b(x) dx .$$

4.4 Quantum Mechanical Treatment of Dipole Scattering

The quantum mechanical approach utilizes perturbation theory to calculate the transition electric dipole. The transition electric dipole is then used to replace the induced electric dipole, and describes the transition polarizability for transitions from an initial state $|i\rangle$ to final a state $\langle f |$ for a given excitation frequency, generally excited by laser frequency. The transition dipole can be described as a sum of individual components where each corresponds to different dependencies on the applied electric field,

$$p_{fi} = \left(p^1\right)_{fi} + \left(p^2\right)_{fi} + \left(p^3\right)_{fi} + \ldots,$$

where the subscript *fi* represents the transition from the initial to the final state. By applying perturbation theory, we can use the bra-ket notation to represent the total transition dipole as,

$$p_{fi} = \langle \Psi_f' | \hat{p} | \Psi_i' \rangle,$$

where,

Ψ_f' is the perturbed time-dependent wave function for the final state,

Ψ_i' is the perturbed time-dependent wave function for the initial state, and

$\hat{p}$ is the electric dipole moment operator.

Through the use of perturbation theory, it is possible to derive expressions for the transition dipole by expressing each term as a linear combination of unperturbed and perturbed states [Long, 2001]. In the case of the electric dipole operator, we can write,

$$\left(p^1\right)_{fi} = \left\langle \Psi_f^0 \left| \hat{p} \right| \Psi_i^1 \right\rangle + \left\langle \Psi_f^1 \left| \hat{p} \right| \Psi_i^0 \right\rangle .$$

The value is linearly dependent on the applied electric field because each portion is dependent only on a single perturbed state, either Ψ_i^1 or Ψ_f^1.

4.5 Theory of Resonant-Enhanced Raman Scattering

The experiments performed in my research were carried out using an arrangement with a 90° scattering angle between the incident beam and the collection paths. For a Raman scattering transition between the initial state $\left| i \right\rangle$ and final state $\left\langle f \right|$, the intensity of the scattered light at 90° with respect to the excitation beam is given by,

$$I_{fi}\left(\frac{\pi}{2}\right) = \frac{\pi^2}{\varepsilon_0^2}\left(\tilde{\nu}_0 \pm \tilde{\nu}_{fi}\right)^4 I_0 \sum_{\rho,\sigma}\left[\left[\alpha_{\rho\sigma}\right]_{fi}\left[\alpha_{\rho\sigma}\right]_{fi}^*\right]$$

where ,

$\tilde{\nu}_0$ is the wavenumber of the excitation laser,

$\tilde{\nu}_{fi}$ is the wavenumber of the Raman transition $\left\langle f \right| \leftarrow \left| i \right\rangle$,

$\tilde{\nu}_0 + \tilde{\nu}_{fi}$ is the wavenumber of the Raman anti-Stokes scattered radiation,

$\tilde{\nu}_0 - \tilde{\nu}_{fi}$ is the wavenumber of the Raman Stokes scattered radiation,

I_0 is the irradiance W/m^2 of the incident radiation,

ε_0 is the permittivity of free space, 8.854 $\times 10^{-12}$ F/m,

and $[\alpha_{\rho\sigma}]_{fi}$ is the ρσth element of the transition polarizability tensor as given by the Kramers—Heisenberg Dispersion Formula [Kramers & Heisenberg, 1925], and is written as,

$$[\alpha_{\rho\sigma}]_{fi} = \frac{1}{hc} \sum_{r \neq i,f} \left[\frac{[\mu_\rho]_{fr}[\mu_\sigma]_{ri}}{\tilde{\nu}_{ri} - \tilde{\nu}_o - i\Gamma_r} + \frac{[\mu_\sigma]_{fr}[\mu_\rho]_{ri}}{\tilde{\nu}_{rf} + \tilde{\nu}_o + i\Gamma_r} \right] \qquad [4.4]$$

where,

$[\mu_\rho]_{fr}$ is the ρ^{th} component of the transition dipole moment associated with the transition $\langle f | \leftarrow | r \rangle$,

$[\mu_\sigma]_{fr}$ is the σ^{th} component of the transition dipole moment associated with the transition $\langle f | \leftarrow | r \rangle$, and

$i\Gamma_r$ is the damping factor that is inversely proportional to the lifetime of state $|r\rangle$.

In the case of resonance-enhanced Raman scatter, the excitation laser frequency, $\tilde{\nu}_0$, is tuned to a frequency near the electronic absorption frequency, $\tilde{\nu}_{ri}$, and as $\tilde{\nu}_0$ approaches $\tilde{\nu}_{ri}$, $\tilde{\nu}_{ri} - \tilde{\nu}_o$ approaches 0. Tuning reduces the denominator of the first term of the polarizability tensor, and results in large increase in the efficiency of the transition. This increase in the polarizability tensor represents the process by which the normally weak Raman scattered signal is enhanced in the resonance process.

Examination of the polarizability tensor, $\left[\alpha_{\rho\sigma}\right]_{fi}$, helps our understanding of this enhancement. Under resonance conditions, the 2nd term in the transition polarizability (Equation 4.4) can be neglected, yielding,

$$\left[\alpha_{\rho\sigma}\right]_{fi} \cong \frac{1}{hc}\sum_{r\neq i,f}\frac{\left[\mu_{\rho}\right]_{fr}\left[\mu_{\sigma}\right]_{ri}}{\tilde{\nu}_{ri}-\tilde{\nu}_{o}-i\Gamma_{r}}. \qquad [4.5]$$

A convenient and commonly used simplification is the Born–Oppenheimer approximation, which is a method for separating the response of the nuclei from that of the electrons. Because the nuclei have significantly more inertia than the electrons, the relative response of the nuclei to the applied field can be neglected, and therefore only the response of the electron distribution needs to be considered. This approximation allows the excited states to be separated into products of vibrational and electronic states, that is,

$$\begin{aligned}
\left|i\right\rangle &= \left|e_i\nu_i\right\rangle = \left|e_i\right\rangle\left|\nu_i\right\rangle,\\
\left|r\right\rangle &= \left|e_r\nu_r\right\rangle = \left|e_r\right\rangle\left|\nu_r\right\rangle,\\
\left|f\right\rangle &= \left|e_f\nu_f\right\rangle = \left|e_f\right\rangle\left|\nu_f\right\rangle,
\end{aligned}$$

where e and ν represent the electronic and vibrational states for the initial (i), virtual (*r*), and final (*f*) states. Typically the initial and final electronic states are the ground state that further simplifies to,

$$\begin{aligned}
\left|i\right\rangle &= \left|g\nu_i\right\rangle = \left|g\right\rangle\left|\nu_i\right\rangle\\
\left|r\right\rangle &= \left|e_r\nu_r\right\rangle = \left|e_r\right\rangle\left|\nu_r\right\rangle\\
\left|f\right\rangle &= \left|g\nu_f\right\rangle = \left|g\right\rangle\left|\nu_f\right\rangle.
\end{aligned}$$

For this case, Equation [4.5] can be rewritten as,

$$\left[\alpha_{\rho\sigma}\right]_{fi} \cong \frac{1}{hc}\sum_{r\neq i,f}\frac{\left\langle\nu_f\right|\left[\mu_{\rho}\right]_{ge}\left|\nu_r\right\rangle\left\langle\nu_r\right|\left[\mu_{\sigma}\right]_{eg}\left|\nu_i\right\rangle}{\tilde{\nu}_{ri}-\tilde{\nu}_{o}-i\Gamma_{r}}, \qquad [4.6]$$

where $[\mu_\rho]_{ge}$ is the ρ^{th} component of the transition dipole moment for the electronic transitition $|g\rangle \leftarrow |e\rangle$ [Dines, 2008].

Finally by applying the Herzberg-Teller [Herzberg and Teller, 1933] expansion to the transition polarizability tensor, one can separate the Raman scattering into what is known as the *A*, *B*, *C*, and *D* terms of the transition polarizability [Long, 2001].

$$\left[\alpha_{\rho\sigma}\right]_{fi} = \left[\alpha_{\rho\sigma}\right]_{fi}^{A} + \left[\alpha_{\rho\sigma}\right]_{fi}^{B} + \left[\alpha_{\rho\sigma}\right]_{fi}^{C} + \left[\alpha_{\rho\sigma}\right]_{fi}^{D}$$

The four terms are included for completeness, although the *C* and *D* terms are likely to be very small in magnitude [Long, 2001] and are usually ignored in both Raman scattering and resonance enhanced Raman scattering.

***A* – Term:** In applying the Franck-Condon approximation the polarizability is determined by the electronic transition dipole moment, $\lfloor \mu_\rho \rfloor$, and the vibrational overlap integral [Long, 2001], and is given by,

$$\left[\alpha_{\rho\sigma}\right]_{fi}^{A} = \frac{1}{hc}\left[\mu_\rho\right]_{ge}^{0}\left[\mu_\sigma\right]_{eg}^{0}\sum_{r\neq i,f}\frac{\left\langle \nu_f^{(g)} \middle| \nu_r^{(e)} \right\rangle \left\langle \nu_r^{(e)} \middle| \nu_i^{(g)} \right\rangle}{\tilde{\nu}_{ri} - \tilde{\nu}_o - i\Gamma_r} \quad . \qquad [4.7]$$

***B* – Term:** This term represents the vibronic coupling of the resonant excited state, $\left| \nu_e^r \right\rangle$, to one other excited state, $\left| \nu_e^s \right\rangle$ [Long, 2001],

$$\begin{aligned}\left[\alpha_{\rho\sigma}\right]_{fi}^{B} = {} & \frac{1}{h^2c^2}\left[\mu_\rho\right]_{ge}^{0}\left[\mu_\sigma\right]_{eg}^{0}\frac{h_{se}^{k}}{\Delta\tilde{\nu}_{es}}\sum_{r\neq i,f}\frac{\left\langle \nu_f^{(g)} \middle| Q_k \middle| \nu_r^{(e)} \right\rangle \left\langle \nu_r^{(e)} \middle| \nu_i^{(g)} \right\rangle}{\tilde{\nu}_{ri} - \tilde{\nu}_o - i\Gamma_r} \\ & + \frac{1}{h^2c^2}\left[\mu_\rho\right]_{ge}^{0}\left[\mu_\sigma\right]_{eg}^{0}\frac{h_{es}^{k}}{\Delta\tilde{\nu}_{se}}\sum_{r\neq i,f}\frac{\left\langle \nu_f^{g} \middle| \nu_r^{(e)} \right\rangle \left\langle \nu_r^{(e)} \middle| Q_k \middle| \nu_i^{(g)} \right\rangle}{\tilde{\nu}_{ri} - \tilde{\nu}_o - i\Gamma_r} \quad . \end{aligned} \qquad [4.8]$$

***C* – Term:** This term represents the **v**ibronic coupling of the ground electronic state , $\left|\nu_e^g\right\rangle$, to an excited electronic state , $\left|\nu_e^t\right\rangle$ [Long, 2001],

$$\left[\alpha_{\rho\sigma}\right]_{fi}^{C} = \frac{1}{h^2c^2}\left[\mu_\rho\right]_{se}^{0}\left[\mu_\sigma\right]_{eg}^{0}\frac{h_{sg}^{k}}{\Delta\tilde{\nu}_{gs}}\sum_{r\neq i,f}\frac{\left\langle\nu_f^{(g)}\left|Q_k\right|\nu_r^{(e)}\right\rangle\left\langle\nu_r^{(e)}\left|\nu_i^{(g)}\right\rangle\right.}{\tilde{\nu}_{ri}-\tilde{\nu}_o-i\Gamma_r} + \frac{1}{h^2c^2}\left[\mu_\rho\right]_{ge}^{0}\left[\mu_\sigma\right]_{eg}^{0}\frac{h_{gs}^{k}}{\Delta\tilde{\nu}_{sg}}\sum_{r\neq i,f}\frac{\left\langle\nu_f^{(g)}\left|Q_k\right|\nu_r^{(e)}\right\rangle\left\langle\nu_r^{(e)}\left|\nu_i^{(g)}\right\rangle\right.}{\tilde{\nu}_{ri}-\tilde{\nu}_o-i\Gamma_r}. \quad [4.9]$$

***D* – Term:** Vibronic coupling of the excited electronic state, $\left|\nu_e^r\right\rangle$,to two other excited electronic states , $\left|\nu_e^s\right\rangle$ and $\left|\nu_e^{s'}\right\rangle$ [Long, 2001] is represented,

$$\left[\alpha_{\rho\sigma}\right]_{fi}^{D} = \frac{1}{h^3c^3}\left[\mu_\rho\right]_{gs}^{0}\left[\mu_\sigma\right]_{eg}^{0}\frac{h_{se}^{k}}{\Delta\tilde{\nu}_{es}}\frac{h_{es}^{k}}{\Delta\tilde{\nu}_{se}}\sum_{r\neq i,f}\frac{\left\langle\nu_f^{(g)}\left|Q_k\right|\nu_r^{(e)}\right\rangle\left\langle\nu_r^{(e)}\left|Q_k\right|\nu_i^{(e)}\right\rangle}{\tilde{\nu}_{ri}-\tilde{\nu}_o-i\Gamma_r}. \quad [4.10]$$

4.6 Qualitative Description of the A and B Terms for Resonance-Raman Scattering

The *A*-term, or the Franck–Condon resonance-Raman effect, is determined by convolving the pure electronic transition dipole moment with the vibrational overlap integrals. The *A*-term resonance-Raman scattering occurs when two conditions are met [Long, 2001]:

1. The transition dipole moments $\left[\mu_\rho\right]_{ge}^{0}$ and $\left[\mu_\sigma\right]_{eg}^{0}$ must be non-zero [Clark and Dines, 1986], and
2. The products of the vibrational overlap integrals (Franck-Condon factors), $\left\langle\nu_f^{(g)}\left|\nu_r^{(e)}\right\rangle\left\langle\nu_r^{(e)}\right|\nu_i^{(g)}\right\rangle$, must be nonzero for at least some value of the vibrational quantum state, ν [Clark and Dines, 1986].

The first condition is met if the resonant electronic transition is electric-dipole-allowed. This is generally the case when a strong absorption band results from a π-π^* transition, or from charge transfer [Clark and Dines, 1986]. The second condition is met if there is a difference in the vibrational energy between the ground state levels, $\left|\nu_i^{(g)}\right\rangle$, and the electronic excited states, $\left|\nu_i^{(e)}\right\rangle$, resulting in a change of the shape of the potential field, or if there is a displacement ΔQ_k in the minimum of the excited potential field of the electronic states with respect to the normal coordinate Q_k. [Clark and Dines, 1986]. Figure 4.1 displays a diagram of the conditions that represent four possible cases associated with the occurrence of A-term resonance-Raman scattering.

In Figure 4.1(a), there is neither a change in the potential shape, nor a change in the potential minimum, therefore there is no *A*-term scattering. Figure 4.1(b) shows a change in the potential shape resulting in non-zero vibrational overlap integrals for both totally symmetric and asymmetric modes. The cases shown in Figures 4.1(c) and (d) represent the excitation associated with non-zero overlap integrals for totally symmetric modes with a displacement in the potential field. In practice a significant change in the vibrational energy state occurs only when there is a displacement of the potential energy minimum, therefore case (d) is considered most important [Clark and Dines, 1986]. If the displacement of the potential minimum is large enough, then the *A*-term resonant Raman scattering can result in overtones with intensities that are comparable to the fundamental.

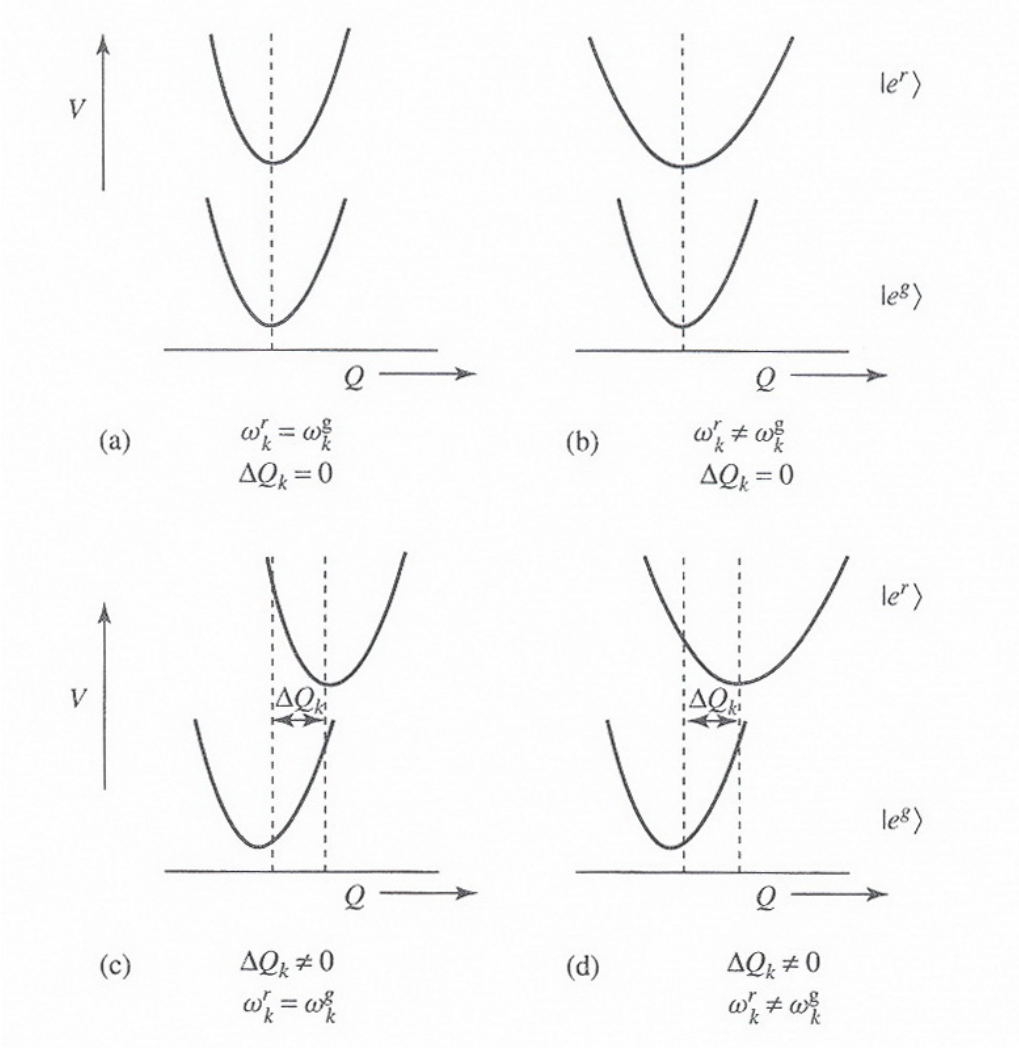

Figure 4.1. Four conditions for *A*-term scattering [Long, 2001].

The *B*-term resonant scattering is the result of vibronic coupling of the resonant excited state $\left|\nu_e^r\right\rangle$,to one other excited state $\left|\nu_e^s\right\rangle$ [Long, 2001]. Similar to the *A*-term, the *B*-term depends on non-zero overlap and transition integrals, as well as on the intensity of the vibronic coupling h_{se}^k and upon the difference between the coupled states $\Delta\tilde{\nu}_{es}$. The *B*-term is usually smaller than the *A*-term, however if the resonant transition yields zero, or near zero displacements of the potential minimum then only the diagonal overlap integrals are non-zero and as such the *A*-term is

vanishing. [Clark and Dines, 1986]. For times when the A-term is zero, the *B*-term may be the only significant contribution to the resonance Raman scattering, and in this case the diagonal overlap integrals are important. These integrals are only non-zero for $\nu_i^{(g)} = \pm 1$; therefore only fundamental Raman shifts are observed, so that there are no overtones. An extension of this idea, known as the 'low temperature limit', occurs when upper vibrational levels are not populated. Thus, $\nu_i^{(g)} = 0_i^{(g)}$ and $\nu_f^{(g)} = 1_f^{(g)}$, and only these two products contribute. In this case, we can remove the summation over the terms in *B*-term from the vibrational overlap integrals [Long, 2001] yielding,

$$\left[\alpha_{\rho\sigma}\right]_{fi}^{B} = \frac{1}{h^2c^2}\left[\mu_\rho\right]_{ge}^{0}\left[\mu_\sigma\right]_{eg}^{0}\frac{h_{se}^{k}}{\Delta\tilde{\nu}_{es}}\frac{\left\langle 1_f^{(g)}\middle|Q_k\middle|0_r^{(e)}\right\rangle\left\langle 0_r^{(e)}\middle|0_i^{(g)}\right\rangle}{\tilde{\nu}_{ri}-\tilde{\nu}_o-i\Gamma_r} + \frac{1}{h^2c^2}\left[\mu_\rho\right]_{ge}^{0}\left[\mu_\sigma\right]_{eg}^{0}\frac{h_{es}^{k}}{\Delta\tilde{\nu}_{se}}\frac{\left\langle 1_f^{g}\middle|1_r^{(e)}\right\rangle\left\langle 1_r^{(e)}\middle|Q_k\middle|0_i^{(g)}\right\rangle}{\tilde{\nu}_{ri}-\tilde{\nu}_o-i\Gamma_r}. \quad [4.11]$$

4.7 Summary

The intensity of non-resonance Raman scattered lines depends on the intensity of the incident radiation, the fourth power of the frequency, and the magnitude of the transition polarizability tensor $\left[\alpha_{\rho\sigma}\right]_{fi}$. The magnitude of the transition polarizability tensor is controlled by the overlap integrals, and their contribution is even more important in the case of resonance-Raman scattering. In the resonance Raman case the proximity of the excitation frequency to the electronic absorption peak $\left(\tilde{\nu}_{ri}-\tilde{\nu}_o\right)$ provides the resonance coupling enhancement. As the excitation frequency approaches the absorption frequency, a minimum in the denominator occurs that

results in the large enhancements of the resonant Raman scattered intensity. The *A*-term resonance Raman scattering results in the observation of strong fundamental line intensities, and can also result in equally strong overtones in the Raman spectra. The *B*-term resonance Raman scattering is limited to fundamental modes and is typically a weaker phenomenon. Table 4.1 shows a comparison that summarizes the Raman and resonant-enhanced Raman scattering [Smith and Dent, 2005].

Table 4.1. Summary of Raman and Resonant Raman [Smith and Dent, 2005]

Raman Scattering	**Resonance Raman Scattering**
B-Term effective	*A*- and *B*-term effective
No overtones	Overtones common
More modes observed in the spectrum	Some modes selectively enhanced
No electronic information	Electronic information present
Weak scattering	Stronger scattering